Type-II Core/Shell CdS/ZnSe Nanocrystals: Synthesis, Electronic Structures, and Spectroscopic Properties

Sergei A. Ivanov,*,[†,||] Andrei Piryatinski,[‡] Jagjit Nanda,[†] Sergei Tretiak,[§,||]
Kevin R. Zavadil,[⊥] William O. Wallace,[⊥] Don Werder,[†] and Victor I. Klimov*,[†,||]

Contribution from the C-PCS, Chemistry Division, Center for Nonlinear Studies, Theoretical Division, and Center for Integrated Nanotechnologies, Los Alamos National Laboratory, Los Alamos, New Mexico 87545, and Sandia National Laboratories, Albuquerque, New Mexico 87185

Received November 21, 2006; E-mail: Ivanov@lanl.gov; Klimov@lanl.gov

Abstract: We report a two-step synthesis of highly luminescent CdS/ZnSe core/shell nanocrystals (emission quantum yields up to 50%) that can produce efficient spatial separation of electrons and holes between the core and the shell (type-II localization regime). Our synthesis involves fabrication of cubic-singony CdS core particles that are subsequently overcoated with a layer of ZnSe in the presence of surfactant-ligands in a noncoordinating solvent. Studies of different growth regime of the ZnSe shell indicate that one approach to obtaining high emission efficiencies is through alloying the CdS/ZnSe interface with CdSe, which leads to the formation of an intermediate ZnCdSe layer with a graded composition. We perform theoretical modeling of these core/shell nanocrystals using effective mass approximation and applying first-order perturbation theory for treating both direct electron−hole coupling and the core/shell interface-polarization effects. Using this model we determine the range of geometrical parameters of the core/shell structures that result in a type-II localization regime. We further applied this model to evaluate the degree of electron−hole spatial separation (quantified in terms of the electron−hole overlap integral) based on measured emission wavelengths. We also discuss the potential applicability of these nanocrystals in lasing technologies and specifically the possibility of single-exciton optical gain in type-II nanostructures.

1. Introduction

Modern colloidal techniques allow fabrication of semiconductor nanocrystals (NCs) with almost atomic precision with a variety of compositions and shapes.[1−5] By combining different materials in a single NC one can also produce various types of heterostructures such as core/shell NCs[6−9] or multicomponent hetero-nanorods[10] and tetrapods.[11] The use of heterostructures has been extensively explored in the traditional semiconductor technology, especially in the case of epitaxial quantum wells and superlattices. Semiconductor heterostructures are typically classified as type-I or type-II, depending on the relative alignment of conduction- and valence-band edges of the materials that are combined at the heterointerface. In the type-I structures, both the conduction and the valence band edges of one semiconductor (semiconductor 1 in Figure 1a) are located within the energy gap of the other semiconductor (semiconductor 2 in Figure 1a). In this case, an electron−hole (e−h) pair excited near the interface tends to localize in semiconductor 1, which provides the lowest energy states for both electrons and holes. In the type-II case (Figure 1b), the lowest energy states for electrons and holes are in different semiconductors; therefore, the energy gradient existing at the interfaces tends to spatially separate electrons and holes on different sides of the heterojunction. The corresponding "spatially indirect" energy gap (E_{g12}) is determined by the energy separation between the conduction-band edge of one semiconductor and the valence-band edge of the other semiconductor. For the case shown in Figure 1b, E_{g12} can be related to conduction (U_c) and valence (U_v) band energy offsets at the interface by $E_{g12} = E_{g1} - U_v = E_{g2} - U_c$, where E_{g1} and E_{g2} are the band gaps of semiconductors 1 and 2, respectively.

[†] C-PCS, Chemistry Division, Los Alamos National Laboratory.
[‡] Center for Nonlinear Studies, Theoretical Division, Los Alamos National Laboratory.
[§] Theoretical Division, Los Alamos National Laboratory.
[||] Center for Integrated Nanotechnologies, Los Alamos National Laboratory.
[⊥] Sandia National Laboratories.

(1) Murray, C. B.; Norris, D. J.; Bawendi, M. G. *J. Am. Chem. Soc.* **1993**, *115*, 8706.
(2) Alivisatos, A. P. *Science* **1996**, *271*, 933.
(3) Peng, X. G.; Manna, L.; Yang, W. D.; Wickham, J.; Scher, E.; Kadavanich, A.; Alivisatos, A. P. *Nature* **2000**, *404*, 59.
(4) Manna, L.; Milliron, D. J.; Meisel, A.; Scher, E. C.; Alivisatos, A. P. *Nat. Mater.* **2003**, *2*, 382.
(5) Kumar, S.; Nann, T. *Small* **2006**, *2*, 316.
(6) Hines, M. A.; Guyot-Sionnest, P. *J. Phys. Chem.* **1996**, *100*, 468.
(7) Dabbousi, B. O.; Rodriguez, Viejo, J.; Mikulec, F. V.; Heine, J. R.; Mattoussi, H.; Ober, R.; Jensen, K. F.; Bawendi, M. G. *J. Phys. Chem. B* **1997**, *101*, 9463.
(8) Cao, Y. W.; Banin, U. *Angew. Chem., Int. Ed.* **1999**, *38*, 3692.
(9) Li, J. J.; Wang, Y. A.; Guo, W. Z.; Keay, J. C.; Mishima, T. D.; Johnson, M. B.; Peng, X. G. *J. Am. Chem. Soc.* **2003**, *125*, 12567.
(10) Shieh, F.; Saunders, A. E.; Korgel, B. A. *J. Phys. Chem. B* **2005**, *109*, 8538.
(11) Milliron, D. J.; Hughes, S. M.; Cui, Y.; Manna, L.; Li, J. B.; Wang, L. W.; Alivisatos, A. P. *Nature* **2004**, *430*, 190.
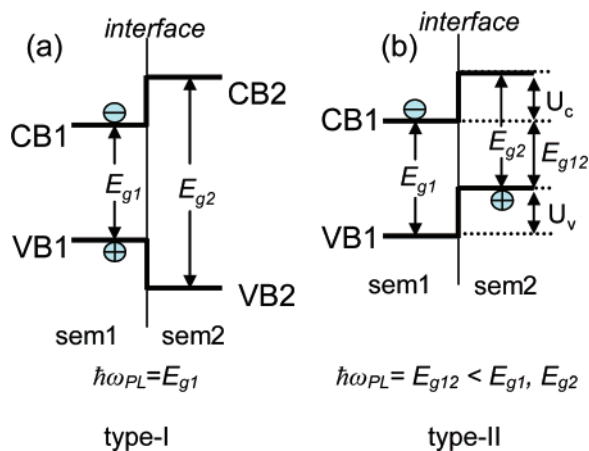
Figure 1. Type-I (a) and type-II (b) band-edge alignments at the heterointerface between two semiconductors. In the type-I structure, both an electron and a hole tend to localize within the material with a narrower energy gap, which is semiconductor 1 (*sem1*) in the present case. As a result, the emission energy, $\hbar\omega_{PL}$, is determined by E_{g1}. The energy gradient existing in the type-II structure tends to spatially separate the electron and the hole on different sides of the heterointerface. In this case, the emission energy is determined by the energy difference between the conduction band edge of *sem1* and the valence band edge of semiconductor 2 (*sem2*), and hence, it is lower than the band gap of either semiconductor.

In the case of colloidal nanostructures, the concept of heterostructuring has been primarily explored in the context of type-I core/shell NCs, in which the shell of a wide-gap semiconductor is used to improve confinement of both an electron and a hole in the core made of a lower-gap material. This approach allows one to reduce interactions of core-localized e–h pairs (excitons) with surface traps, which can result in significant improvements in NC emission quantum yields (QYs).[6–9]

Interesting opportunities are associated with the use of the type-II regime in colloidal structures which could allow, for example, control of both single[12] and multiexciton[13] lifetimes. Furthermore, spatial separation between positive and negative charges produced in these structures can simplify applications of NCs in photovoltaic technologies. Additionally, since the band-edge transition energy in the type-II structure is smaller than the energy gap of either material comprising it (see Figure 1b), the type-II hetero-NCs can be used, e.g., in obtaining infrared emission wavelengths using combinations of well-studied wide-gap semiconductors.[14] Finally, one potentially important application of type-II structures is in NC lasing technologies, where they can be utilized for obtaining optical gain in the low-threshold single-exciton regime[15] without complications associated with multiexciton nonradiative Auger recombination.[16]

Recent demonstrations of type-II colloidal core/shell NCs include such combinations of materials as CdTe/CdSe,[14] CdTe/CdS,[17] CdTe/CdSe,[18] ZnTe/CdS,[19] and ZnTe/CdTe.[19] In all of

these examples, one component of a heterostructure is a Te-based compound. A potential problem associated with a practical use of these structures is the known tendency of Te-containing colloidal nanoparticles toward oxidation, which results in reduced chemical stability. Uncontrolled oxidation also complicates obtaining high emission efficiencies and may require incorporation of additional protection layers (see, e.g., ref 20) that separate the Te-based material from the environment for improving photoluminescence (PL) QYs. The largest reported PL QYs for type-II Te-based hetero-nanoparticles (up to 10–30%) were obtained using this latter approach.[18]

Recently, we explored the use of CdSe and ZnSe, which are more stable in the colloidal form than Te-based semiconductors, for fabricating heterostructures that can exhibit the type-II localization regime.[12,15] In our work we applied an "inverted" core/shell design, in which a core of a wide-gap ZnSe was overcoated with a narrower-gap CdSe. These NCs showed high emission QYs up to 80–90%.[15] An interesting property of these structures was tunability between type-I and type-II regimes that can be achieved by simply varying the shell thickness for a fixed core radius.

While being a useful model system in studies of the effect of spatial separation between electrons and holes on, e.g., carrier recombination dynamics[12,13] and optical-gain properties,[15] "inverted" ZnSe/CdSe NCs can only produce partial spatial separation between electrons and holes. The "charge-separated" state in these nanostructures corresponds to the situation for which the electron is confined to the shell region while the hole is still delocalized over the entire volume of the hetero-NCs, which leads to reduced but nonzero overlap between the electron and the hole wavefunctions. Here, we refer to this localization regime as *quasi type-II*.

The purpose of the current study is the development of core/shell structures that can produce complete separation of negative and positive charges between the core and the shell, which would correspond to the true type-II localization regime. Since one of the applications that we envision for these structures is lasing, two important requirements for them are large emission efficiencies and good photostability. Based on these requirements, we concentrate on heterostructures comprising ZnSe and CdS, both of which are known to exhibit good stability in the colloidal form. Furthermore, our theoretical modeling (see below) indicates that both geometries, ZnSe(core)/CdS(shell) and CdS(core)/ZnSe(shell), allow one to achieve essentially zero overlap between electron and hole wavefunctions (for sufficiently large core radii and shell thicknesses) indicating nearly complete spatial separation between electrons and holes.

In our synthetic work, we focus on CdS-core heterostructures because they are expected to show a transition from the type-I to the type-II regime for smaller shell thicknesses that are easier to fabricate with sufficiently high quality. The targeted structures are produced by a two-step synthesis that involves fabrication and purification of CdS-core particles followed by a deposition of the ZnSe shell. As prepared, these hetero-NCs exhibit relatively high emission QYs up to 10–15%. Further increase in the emission efficiency can be obtained by alloying the core/

(12) Balet, L. P.; Ivanov, S. A.; Piryatinski, A.; Achermann, M.; Klimov, V. I. *Nano Lett.* **2004**, *4*, 1485.
(13) Nanda, J.; Ivanov, S. A.; Htoon, H.; Bezel, I.; Piryatinski, A.; Tretiak, S.; Klimov, V. I. *J. Appl. Phys.* **2006**, *99*, 034309.
(14) Kim, S.; Fisher, B.; Eisler, H.-J.; Bawendi, M. *J. Am. Chem. Soc.* **2003**, *125*, 11466.
(15) Ivanov, S. A.; Nanda, J.; Piryatinski, A.; Achermann, M.; Balet, L. P.; Bezel, I. V.; Anikeeva, P. O.; Tretiak, S.; Klimov, V. I. *J. Phys. Chem. B* **2004**, *108*, 10625.
(16) Klimov, V. I.; Mikhailovsky, A. A.; McBranch, D. W.; Leatherdale, C. A.; Bawendi, M. G. *Science* **2000**, *287*, 1011.
(17) Schöps, O.; Le Thomas, N.; Woggon, U.; Artemyev, M. V. *J. Phys. Chem. B* **2006**, *110*, 2074.

(18) Yu, K.; Zaman, B.; Romanova, S.; Wang, D.; Ripmeester, J. *Small* **2005**, *1*, 332.
(19) Xie, R.; Zhong, X.; Basché, T. *Adv. Mater.* **2005**, *17*, 2741.
(20) Cheng, C.-T.; Chen, C.-Y.; Lai, C.-W.; Liu, W.-H.; Pu, S.-C.; Chou, P.-T.; Chou, Y.-H.; Chiu, H.-T. *J. Mater. Chem.* **2005**, *15*, 3409.

shell interface with small amounts of CdSe which results in QYs up to 50%. The measured emission wavelengths (tunable between 500 and 650 nm) are in good agreement with the band-edge transition wavelengths calculated for the regime where electrons and holes are separated between the core and the shell. By providing both synthetic procedures for fabricating a new class of type-II NCs together with a theoretical model that accurately describes their electronic structures, this work opens interesting opportunities for systematic studies of effects of carrier localization (e.g., different degrees of spatial separation between electrons and holes) on electronic and optical properties of colloidal semiconductor nanostructures.

2. Experimental Section

2.1. Chemicals. Myristic acid (99.5%, Acros), tetraethylthiuram disulfide (97%, Acros), 2,2′-dithiobisbenzothiazole (99%, Acros), Cd(AcO)$_2$·2H$_2$O (98%, Acros), Zn(AcO)$_2$·2H$_2$O (99%, Acros), ZnEt$_2$ (98%, Strem), Se shot (99.9999%, Acros), tri-*n*-octylphosphine (TOP, 97%, Strem), benzoyl peroxide (BPO, 97%, Aldrich), benzylamine (BzNH$_2$, 99%, Acros), phenylphosphonic acid (PhP(O)(OH)$_2$, 98%, Aldrich), and anhydrous hexane (Aldrich), methanol (Aldrich), chloroform (Acros), toluene (Aldrich), and butanol (Aldrich) were used as purchased. Tri-*n*-octylphosphine oxide (TOPO, 90%, Fisher), hexadecylamine (HDA, 98%, Lancaster), octadecylamine (ODA, 90%, Acros), 1-octadecene (ODE, 90%, Acros), and oleic acid (OA, 90%, Aldrich) were used as is but were dried and degassed in a vacuum for 2–3 h at 120 °C shortly before use. All reactions were conducted under a nitrogen atmosphere using the Schlenk technique.

2.2. Characterization. UV–vis absorption spectra were recorded using a Lambda-2 Perkin-Elmer spectrophotometer. PL spectra were taken with a Jobin Yvon Fluorolog-3 fluorescence spectrophotometer using excitation wavelengths of 365 or 460 nm. PL QYs of NC samples were measured relative to organic dyes with known emission efficiencies. The NC PL QY was calculated as $QY_{NC} = QY_{dye}(I_{NC}/I_{dye})(n_{NC})^2/(n_{dye})^2(1 - 10^{-OD_{dye}}/1 - 10^{-OD_{NC}})$, where *I* is the spectrally integrated emission intensity, *n* is the refractive index, and OD is the optical density of the NC or the dye samples (indicated by a subscript). The optical density of the NC samples at the excitation wavelength was within the 0.02–0.05 range. The QY data reported in this work were obtained using Coumarin 510, Coumarin 540A, or DCM as standards with QYs of 85% (in ethanol),[21] 43% (in acetonitrile),[22] and 44% (in acetonitrile),[23] respectively.

X-ray diffraction (XRD) studies of NCs were carried out with a Philips D-5000 diffractometer using Cu Kα radiation. Drop cast films of the NCs were deposited on single crystalline sapphire substrates oriented at a specific angle. A strong single-crystal peak originating from the oriented substrate (2θ value of 25.576°) was excluded from the detector window by proper θ correction. This procedure eliminated any possibility for a background contribution from the substrate to the diffraction signal. Since the NC samples produce very weak diffraction intensities, the XRD data were collected at a slow scan rate (25 s/0.04°) for a better signal-to-noise ratio.

Transmission electron microscopy (TEM) studies were performed using a JEOL 2010 microscope operating at 200 kV. TEM samples were prepared by placing a drop of the NC solution onto a 400 mesh copper grid with an ultrathin carbon film on a holey carbon support (Ted Pella, Inc.). The excess solution was wicked off the grid with a piece of a filter paper. Elemental analysis was performed using an EDAX EDAM III energy dispersive spectrometer with a Si(Li) detector

mounted on a Tecnai G2 30 (S)TEM. FEI TIA software was used to analyze the collected data.

X-ray Photoelectron Spectroscopy (XPS) was performed on Kratos Axis Ultra spectrometer using Mg Kα radiation. Spectra were acquired at a fixed pass energy of 80 eV. The samples for the XPS studies were prepared by drop-casting an NC solution in the MeOH/toluene mixture onto a freshly cleaved, highly ordered pyrolytic graphite (HOPG) substrate. Regions of continuous NC spatial distribution, suitable for making quantitative measurements of particle composition, were first identified by conducting lower energy resolution survey scans.

2.3. Synthesis of CdS Nanocrystals. Synthesis of highly monodisperse cubic CdS NCs was performed according to a recently published method.[24] In a typical procedure, large CdS NCs (ca. 2.5 nm radius) were synthesized as follows. 0.266 g (1 mmol) of Cd(AcO)$_2$·2H$_2$O, 0.4567 g (2 mmol) of myristic acid, 5.14 mL of 0.1 M sulfur solution in ODE (0.514 mmol), 1.3 mL of 0.05 M tetraethylthiuram disulfide solution in ODE (65 μmol), and 0.064 g of 2,2′-dithiobisbenzothiazole (192 μmol) were all placed in a 100 mL flask with 30 mL of ODE and heated in a vacuum for 1 h at 120 °C. Subsequently, the flask with the reaction mixture was filled with N$_2$ and slowly heated (∼6 °C/min) to 240 °C. The solution turned dark yellow as the temperature reached 240 °C. The particle size was monitored by recording UV–vis and PL spectra of growth-solution aliquots in chloroform. For sizes that corresponded to emission wavelengths longer than 470 nm, CdS NCs became insoluble in the reaction mixture (corresponding growth times were 30 min or longer at 240 °C); we also observed that for these larger sizes the solution became turbid. After a desired particle size was reached, the growth solution was cooled down and washed twice with chloroform and toluene to remove byproducts and free ligands; synthesized CdS particles were not soluble in either of the above solvents.

To synthesize smaller CdS nanocrystals (radii from 1.0 to 1.5 nm), the growth solution with the same ratio of reagents was cooled down as soon as its temperature reached 240 °C. These smaller particles were soluble in hydrocarbon solvents, and for purification, they were washed with acetone, redissolved in toluene, and reprecipitated with acetone.

2.4. Purification of CdS NCs with Pyridine. Synthesized CdS NCs required extra purification to ensure that no Cd(II) was left as adsorbate on the NC surface. After precipitation and washing of these NCs with acetone, the solvent was removed *in vacuo* and 5–10 mL of pyridine were added to a vial with 10–20 mg of dry CdS NCs. Stirring the mixture for 12 h at 50 °C lead to full dissolution of NCs in pyridine. The NCs were precipitated from pyridine with water, redissolved in acetone, and again precipitated with water. The washed NCs were dissolved in hexane and used in the synthesis of CdS/ZnSe core/shell structures.

2.5. Overcoating with ZnSe. In a typical overcoating procedure, 20 mg of CdS NCs were dispersed (or dissolved, for smaller sizes) in hexane and injected into a degassed mixture of ODA (1.5 g) and ODE (6 mL) at 120 °C. Following the injection, the solution was placed under a vacuum for 20–30 min to remove hexane. Subsequently, the solution was put back under a N$_2$ atmosphere and was heated to 220–240 °C. Separately, a 0.1 M solution of zinc oleate in TOP was prepared by mixing of Zn(AcO)$_2$ in TOP with the equivalent amount of oleic acid. 4–5 mL of zinc oleate solution were mixed with the stoichiometric amount of 1 M Se solution in TOP and added dropwise to the flask with CdS NCs. The typical rate of the addition was 8–9 mL/h (i.e., 10^{-3} mol of Zn(II)/h), although the rate as low as 2–3 mL/h can be used without inducing apparent changes in the shape and emission quality of final product. Upon Zn/Se addition, the solution color changed from lemon-yellow to red. After the addition, the temperature of the reaction mixture was lowered to 150–170 °C, and the solution was annealed at this temperature for 24–48 h in order to increase the PL QY of formed CdS/ZnSe core/shell NCs. After the annealing, the

(21) Fletcher, A. N.; Bliss, D. E.; Kauffman, J. M. *Opt. Commun.* **1983**, *47*, 57.
(22) Jones, G., II; Jackson, W. R.; Halpern, A. M. *Opt. Commun.* **1980**, *72*, 391.
(23) Drake, J. M.; Lesiecki, M. L.; Camaioni, D. M. *Chem. Phys. Lett.* **1985**, *113*, 530.

(24) Cao, Y. C.; Wang, J. H. *J. Am. Chem. Soc.* **2004**, *126*, 14336.

temperature was lowered to 80−90 °C and CdS/ZnSe NCs were precipitated with acetone and centrifuged. The supernatant was discarded, and the product was washed with MeOH and acetone. After washing and centrifugation, purified NCs were dissolved in toluene or hexane and stored in the dark. The PL QY of CdS/ZnSe NCs after annealing was in the range 10 to 15%. PL QYs of CdS/ZnSe NCs hexane solutions did not change for a week when samples were stored under an inert atmosphere and ambient light. Samples stored in the dark maintained their PL QYs for 1−2 months.

2.6. CdS/ZnSe Interface Alloying. Further increase in the PL QY of CdS/ZnSe NCs can be obtained by alloying the ZnSe layer adjacent to the CdS core with CdSe[25] to produce an intermediate ZnCdSe layer with a graded composition. In a typical alloying procedure, the Cd(AcO)$_2$·2H$_2$O solution in TOP was injected into the CdS NC solution in ODA/ODE prior to addition of the Zn/Se precursors. The amount of extra Cd(II) added to the solution was 1−10% of the molar amount of Zn(II) used in the subsequent shell deposition. A slight excess of Se/TOP (10−20%) compared to the total amount of added Cd(II) and Zn(II) was used. The rest of the ZnSe shell growth procedure was the same as that above. The average PL QYs of moderately alloyed CdS/ZnSe NCs (with 5% Cd(II) added) were 20−25%, whereas the best heavily alloyed samples (with 10% of Cd(II) added) showed PL QYs as high as 50%.

2.7. CdS/ZnSe Etching with BPO. To confirm the core−shell geometry of synthesized nanostructures, we performed the controlled etching of CdS/ZnSe NCs with BPO according to the procedure described in the literature.[26] For efficient and reproducible etching results, the ODA- and TOP-ligands of as-synthesized CdS/ZnSe NCs were exchanged for BzNH$_2$ by a dropwise addition of the amine to the hexane solution of isolated and purified NCs. Initial portions of BzNH$_2$ cause the clear solution of NCs to become cloudy. The addition of the amine was continued until the solution again became clear. BzNH$_2$-exchanged NCs (CdS/ZnSe/BzNH$_2$) were precipitated with hexane, centrifuged, and redissolved in the MeOH/toluene mixture (1:3). 100 μL of 0.3 M solution of BPO in the MeOH/toluene were added directly to a quartz cuvette filled with the CdS/ZnSe/BzNH$_2$ solution right before the cuvette was placed into a spectrophotometer. To improve selectivity of etching, 50 μL of 0.01 M solution of PhP(O)(OH)$_2$ in the MeOH/toluene mixture were added to the cuvette with CdS/ZnSe/BzNH$_2$ before BPO addition. During the etching, UV−vis absorption spectra were acquired with time intervals of 2.5 min, a rate of 2000 nm/min, and a resolution of 1 nm.

2.8. XPS Studies of CdS/ZnSe NCs. During the 2 h ZnSe shell deposition over CdS cores, four 1-mL aliquots of CdS/ZnSe NCs were taken from the growth solution at 10, 45, 90, and 120 min after initiating shell growth. Following initial precipitation with acetone, the CdS/ZnSe NCs were dissolved in 1 mL of hexane and then ligand exchanged with BzNH$_2$ and purified using the procedure described in section 2.7.

3. Theoretical Modeling of Electronic Structures in CdS/ZnSe Nanocrystals

In our earlier studies of "inverted" core(ZnSe)/shell(CdSe) NCs,[12,15] we considered structures in which the bulk heterointerface was characterized by a type-I energy alignment (Figure 1a) and only partial spatial separation between electrons and holes could be obtained. For materials studied here (CdS and ZnSe), the bulk interface is characterized by a type-II alignment of electronic states, which is illustrated in Figure 1b (see also parameters of CdS and ZnSe in Table 1). One can expect that core/shell CdS/ZnSe NCs with a large core radii and a thick shells (quasi-bulk structure) will also correspond to the type-II

(25) Talapin, D. V.; Mekis, I.; Gotzinger, S.; Kornowski, A.; Benson, O.; Weller, H. *J. Phys. Chem. B* **2004**, *108*, 18826.
(26) Battaglia, D.; Blackman, B.; Peng, X. G. *J. Am. Chem. Soc.* **2005**, *127*, 10889.

Table 1. Band Structure Parameters of Bulk CdS and ZnSe[27,28] (Effective Masses Are in Units of Free-Electron Mass)

parameter	CdS	ZnSe
m_e	0.18	0.14
m_h	0.60	0.53
E_g, eV	2.45	2.72
U_e, eV	0.80	
U_h, eV	0.52	

regime (for both CdS-core and ZnSe-core geometries), because in this case, the positions of the lowest-energy quantized levels approach those of the bulk-semiconductor band edges. Therefore, using these NCs one should be able to achieve nearly complete spatial separation between the electron and the hole wavefunctions.

In contrast to bulk or quasi-bulk situations, the regime of carrier localization in the case of small core radii (R) and shell widths (H) becomes dependent on the exact geometry of the NC. Specifically, it can change from type-I (both carriers are delocalized over the entire volume of the hetero-NC), to quasi type-II (one carrier is still delocalized over the entire hetero-NC volume while the other one resides primarily either in the core or in the shell), and finally to the true type-II (electrons and holes are separated between the core and the shell). In our studies, we use the "energy criterion" for defining boundaries between these localization regimes. Specifically, in the case of CdS(core)/ZnSe(shell) heterostructures, we assume that an electron is primarily localized in the core if its lowest-energy (1S) level is located below the conduction-band energy offset (U_c) at the core/shell interface (i.e., electron confinement energy ΔE_e is smaller than U_c). On the other hand, a hole is shell-localized if its confinement energy (ΔE_h) is smaller than the valence-band energy offset (U_v).

Figure 2 illustrates changes in carrier localization that occur in the CdS-core hetero-NC with increasing shell thickness. We consider the situation for which the CdS-core size is relatively large ($R > R_c$, R_c is a critical radius for electron localization in the core) so that the lowest-energy electron level is below the core/shell energy offsets. In this case, the electron is immediately "locked" in the core for any shell thickness (increase in H only lowers the electron 1S level further down; compare panels a and b in Figure 2). The regime of hole localization is, however, dependent upon the value of H. For thin shells, the 1S hole level is above the U_v offset, and hence, the hole wavefunction is delocalized over the entire hetero-NC (Figure 2b). This situation corresponds to partial charge separation (quasi type-II regime) in which only one carrier (electron in this case) is confined to a certain region of a heterostructure. The true type-II regime occurs for shell widths that are greater than a certain critical value, $H_c = H_c(R)$, which can be determined from the energy criterion: $\Delta E_h = U_v$, where ΔE_h is the hole energy measured with respect to the bottom of the valence band. For $H > H_c$, the hole level shifts below the U_v offset and hence the hole becomes shell-localized, which corresponds to the transition to a true type-II regime. In this case, the emission energy, $\hbar\omega_{PL}$ ($\hbar$ is Planck's constant), is determined by a spatially indirect transition, which couples the core-localized conduction-band state to the shell-localized valence-band state.

In our theoretical modeling, we consider small-size NCs, for which carrier confinement energies are much greater than Coulomb interaction energies and hence the latter can be treated
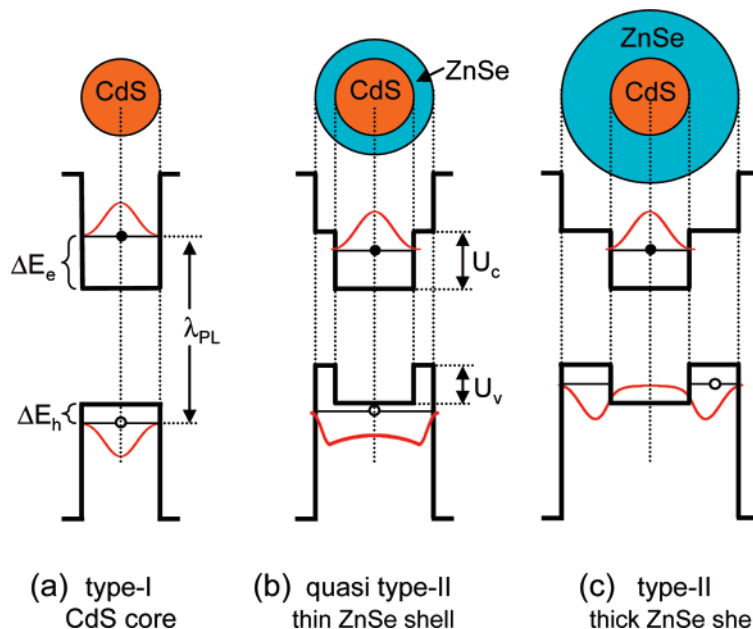
Figure 2. Different localization regimes supported by CdS(core)/ZnSe(shell) NCs as a function of shell thickness, H. (a) Bare CdS-core NCs ($H = 0$) correspond to type-I localization, for which electron and hole wavefunctions (shown by red lines) have identical spatial distributions and, hence, the e−h overlap integral, Θ, is unity. (b) Core/shell NCs with thin shells ($0 < H < H_c$, $R > R_c$) correspond to the quasi type-II regime, in which the electron is localized in the core but the hole is delocalized over the entire NC volume. These structures produce partial separation between electrons and holes, which results in reduced values of Θ ($0.7 < \Theta < 1$). (c) Hetero-NCs with thick shells ($H > H_c$, $R > R_c$) can produce the true type-II regime, for which electrons and holes are separated between the core and the shell. For these charge-separated states, the e−h overlap integral can approach zero.

using perturbation theory.[29] We first derive electron and hole wavefunctions by solving the envelope-function Schrödinger equation for noninteracting electrons and holes using boundary conditions according to which the radial wavefunction is finite at the center of the core and is zero outside the shell. An additional boundary condition is imposed by a requirement of continuity of a current at the core/shell interface, which translates into a requirement for continuity of both the radial wavefunctions and their effective-mass-weighted derivatives at the heterointerface.[30] In our calculations, we only consider the lowest-energy, zero-angular-momentum, conduction- and valence-band 1S states. After finding a solution of the Schrödinger equation, we calculate the Coulomb correction to the energy of a single e−h pair state (single-exciton state) using the first-order perturbation theory, which accounts for the e−h interaction. In these calculations, we consider both direct carriers Coulomb coupling, core/shell and the shell/environment interface polarization effects.

As a quantitative measure of spatial separation between electrons and holes in a hetero-NC, we use an overlap integral between electron and hole wavefunctions defined as $\Theta = |\int_0^{R+H} r^2 \, \mathcal{R}^e(r) \, \mathcal{R}^h(r) \, dr|^2$, where r is the radial coordinate with the origin at the core center and $\mathcal{R}^{e(h)}(r)$ is the radial part of the electron (hole) envelope wavefunction. The overlap integral also determines the strength of the interband 1S(e)−1S(h) optical transition. Details of our modeling can be found in the Supporting Information.

Using the model described above along with each material's parameters listed in Table 1, we derive contour plots of the

(27) *Landolt-Boernstein: Numerical Data and Functional Relationships in Science and Technology. Group III, Condensed Matter, Subvolume C*; Martienssen, W., Editor-in-Chief; Springer: Verlag, 1998.
(28) Dinger, A.; Petillon, S.; Grün, M.; Hetterich, M.; Klingshirn, C. *Semicond. Sci. Technol.* **1999**, *14*, 595.
(29) Efros, Al. L.; Efros, A. L. *Sov. Phys. Semicond.* **1982**, *16*, 772.
(30) Haus, J. W.; Zhou, H. S.; Honma, I.; Komiyama, H. *Phys. Rev. B* **1993**, *47*, 1359.

1S(e)−1S(h) transition wavelength (emission wavelength), $\lambda_{11} = 2\pi c/\omega_{11} = \lambda_{PL}$ (c is the speed of light), and the e−h overlap integral of a hetero-NC as a function of core emission wavelength, λ_o (is directly related to core radius, R), and shell thickness (Figure 3a and 3b, respectively). The use of λ_o instead of R simplifies the comparison of the modeling results with experimental data and also allows us to focus on the effect of the shell thickness on electronic energies while minimizing the role of a systematic difference between the computed and the measured energy gaps of a core, typical for effective-mass calculations. In the same plots, we also show boundaries between different localization regimes (type-I, quasi type-II, and type-II). In the type-I regime, which corresponds to $H < H_c(R)$ and $R < R_c(H)$ (R_c is derived from the condition $\Delta E_e = U_c$), the emission wavelength exhibits strong dependence on both λ_o (hence, core radius) and shell thickness. In the quasi type-II regime ($R > R_c$ and $H < H_c$, or $R < R_c$ and $H > H_c$), λ_{11} is primarily dependent on H and shows only a weak dependence on λ_o. In the type-II regime ($R > R_c$ and $H > H_c$), the emission wavelength is dependent on H for smaller shell widths, however, this dependence saturates for thicker shells when λ_{11} becomes primarily determined by the core radius. In this case, the 1S hole state approaches the bulk ZnSe band edge and the "saturated" value of the emission energy can be estimated from the expression $\hbar\omega_{11}^{sat} \approx E_{g12} + \Delta E_e + V_{eh}$ that is equivalent to $\hbar\omega_{11}^{sat} \approx E_{gCdS} - U_v + \Delta E_e + V_{eh}$, where V_{eh} is the Coulomb correction, which accounts for the e−h interaction energy (see eq 13 in the Supporting Information).
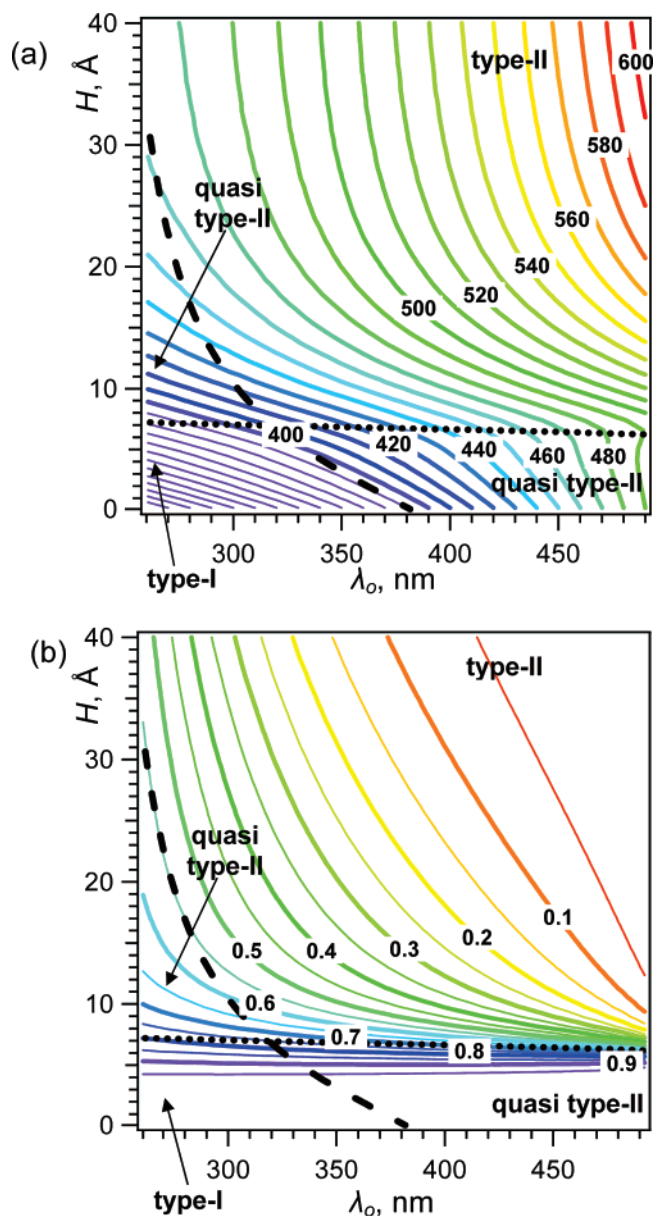
It is illustrative to examine the e−h overlap values that correspond to different localization regimes (Figure 3b). In the range of R and H that correspond to the type-I regime, the Θ values are close to unity ($0.7 < \Theta \leq 1$). At the boundaries that correspond to the transition to type-II localization, $\Theta = 0.65-0.7$ for $H = H_c$ and $\Theta = 0.55-0.65$ for $R = R_c$, and it rapidly decreases with increasing R (increasing λ_o) and/or H. For

Figure 3. Contour plots of the emission wavelength in nm (a) and the e−h overlap integral (b) calculated for CdS/ZnSe core/shell NCs as a function of CdS core emission wavelength, λ_o, and ZnSe shell thickness, H. Black dotted and dashed lines indicate the boundaries between type-I, quasi type-II, and true type-II regimes. These boundaries are calculated using the "energy criterion" described in the text. The increments between adjacent contour lines are 10 nm in (a) and 0.05 in (b).

oscillator strength of the band-edge optical transition is one of the spectroscopic signatures of the type-II regime.

In our modeling, we also considered the case of ZnSe(core)/CdS(shell) NCs. Our calculations indicate that in these structures the drop of the overlap integral (i.e., transition to the type-II regime) with increasing shell thickness occurs more slowly than that in CdS-core hetero-NCs. In ZnSe-core systems, type-II localization is achieved by trapping a relatively light electron within the shell, which requires a deeper potential well (and hence, greater H) than in the case of heavier holes. Based on the above considerations and taking into account the fact that thinner shells are less challenging from the fabrication point of view, our experimental studies concentrate on CdS(core)/ZnSe (shell) NCs. This geometry is also expected to produce more stable structures compared to the ZnSe-core NCs because ZnSe is less prone to oxidation than CdS.

4. Experimental Results and Discussion

4.1. Fabrication of CdS Core Particles: Role of Purification. To fabricate CdS core particles, we used a one-pot synthesis recently reported.[24] In addition to producing narrowly disperse samples, this method also results in NCs with a *cubic* crystalline structure. This is expected to facilitate the growth of a shell of ZnSe, which is also characterized by a *cubic* crystal lattice. One important observation made during our studies of various growth regimes was the significant influence of purity of CdS cores on properties of final CdS/ZnSe structures. Specifically, we observed that incomplete purification of CdS cores after their synthesis gave rise to emission wavelengths of the core/shell NCs that were longer by 30 to 40 nm compared to those predicted by our calculations. A possible reason for this red shift was uncontrolled growth of an interfacial layer of CdSe after addition of Zn/Se precursors. This process could occur due to the presence of Cd(II) species adsorbed on CdS core surfaces and would be thermodynamically more favorable than the growth of a ZnSe layer.

In order to produce hetero-NCs with a well-defined, "sharp" core/shell interface, we used CdS-core particles that were thoroughly purified by triple precipitation from pyridine. This procedure ensures complete removal of surface-adsorbed Cd-(II) complexes. To confirm this, we heated both pyridine-purified and unpurified CdS cores with an excess of TOPSe in an ODA/ODE mixture at 200 °C for 1 h. No changes in absorption or emission spectra of purified CdS NCs were observed, indicating *no* Cd(II) leaching from the core to form CdSe on the NC surface. On the other hand, similar treatment of CdS cores that were only once precipitated with acetone and once washed with hexane and acetone caused the appearance of a red tail in the absorption spectrum, indicating the formation of an outer layer of CdSe due to the reaction of TOPSe with surface-bound Cd(II). Finally, the purified CdS NCs produced core/shell structures with emission wavelengths that accurately matched those calculated for well-defined CdS/ZnSe NCs (the observed deviations were less than 15 nm; see discussion below).

We also studied ZnSe shell growth in the regimes that utilized unpurified or "partially purified" cores. The use of unpurified CdS particles right from the reaction mixture resulted in CdS/ZnSe core/shell NCs that were not highly emissive (QY < 5%). Furthermore, their emission wavelength could not be tuned to wavelengths longer than 510−520 nm despite the use of large

example, for $\lambda_o = 470$ nm (this is one of the samples studied experimentally), the overlap integral drops down to 0.2 (almost complete separation between electron and hole wavefunctions) for the shell thickness of 0.93 nm, which is only a 0.3 nm increase compared to H_c ($H_c = 0.63$ nm for cores with $\lambda_o = 470$ nm). The decrease in Θ becomes even faster for larger core radii (i.e., greater λ_o), and for example, for $\lambda_o = 490$ nm the value Θ = 0.2 can be achieved with the 0.8-nm shell. The drop in Θ during the transition to the type-II regime indicates an increasing degree of spatial separation between electrons and holes that can be described in terms of formation of *spatially indirect* excitons. The optical transition, which corresponds to these indirect excitons, is characterized by a low oscillator strength, which is directly proportional to Θ. Reduction in the

amounts of Zn/Se precursors at various reaction temperatures. These observations indicated that under these conditions the shell growth was significantly slower than in the case of well-purified core particles and appears completely stopped after reaching a certain thickness. A possible reason for this behavior was that ligands used in the synthesis of CdS cores rendered the CdS surface and/or Zn precursor less reactive, which impeded the ZnSe shell formation in the case of unpurified core particles.

For a "partial purification", large CdS NCs that are not soluble in common organic solvents were washed consecutively several times with methanol, acetone, and toluene and centrifuged after each washing. Small CdS NCs that were soluble in nonpolar solvents were precipitated twice with acetone out of the toluene solution with an intermediate washing with methanol. This purification technique is likely to remove primarily ligand molecules ("inhibitors" of shell growth) but leave a significant amount of Cd(II) on NC surfaces. The use of these partially purified cores produced core/shell NCs with high emission efficiencies (20−25%) that were greater than those of hetero-NCs with a sharp core/shell interface. This improvement of the quantum yield was likely due to reduction in the number of the core/shell-interface defects as a result of smoothing the boundary between CdS and ZnSe (see section 2.5).

4.2. ZnSe Shell Growth: Choice of Ligands and Precursors. To overcoat CdS cores with ZnSe we used a TOPO-free environment. Although most of the previous methods for overcoating CdSe NCs with ZnSe or ZnS involved the use of TOPO, we found that the presence of this ligand in the synthesis of CdS/ZnSe heterostructures led to a weaker band edge emission (QYs of 10−15%) compared to samples synthesized in the ODA/ODE environment (QYs of 25−30%). Also, as a source of Zn(II), we used $Zn(OA)_2$ instead of the more traditional $ZnEt_2$, because the latter precursor resulted in only weakly luminescent hetero-NCs. It is likely that high reactivity of $ZnEt_2$ led to the formation of the low-quality ZnSe shell. Commonly, metal carboxylates, such as $Zn(OA)_2$, are employed by predissolving metal oxides in carboxylic acid solutions.[31] However, we found that *in situ* formation of $Zn(OA)_2$ upon dissolution of $Zn(AcO)_2$ in the presence of OA eliminates an extra step in the synthesis without any adverse effect on the reaction product. It is noteworthy that no formation of homogeneous ZnSe NCs was observed with the use of either $ZnEt_2$ or $Zn(OA)_2$ under reaction conditions used here.

4.3. Microstructural and Spectroscopic Characterization of CdS/ZnSe Nanocrystals. Figure 4 shows examples of TEM images of initial CdS core particles (panel a) and resulting core/shell structures [panels b (low-resolution image) and c (high-resolution image)] fabricated by overcoating CdS seeds with ZnSe at 230 °C. While CdS particles are nearly spherical with narrow size dispersion (core diameters are 4.8 ± 0.5 nm), the final hetero-NCs have irregular shapes as was previously observed for other types of core/shell structures.[32,33] Because of the little difference between electron scattering cross-sections of CdS and ZnSe, the core/shell interface is not discernible even in a high-resolution TEM image (Figure 4c). However, the NC size clearly increases following deposition of the shell, and elemental analysis using Energy-Dispersive X-ray Spectroscopy
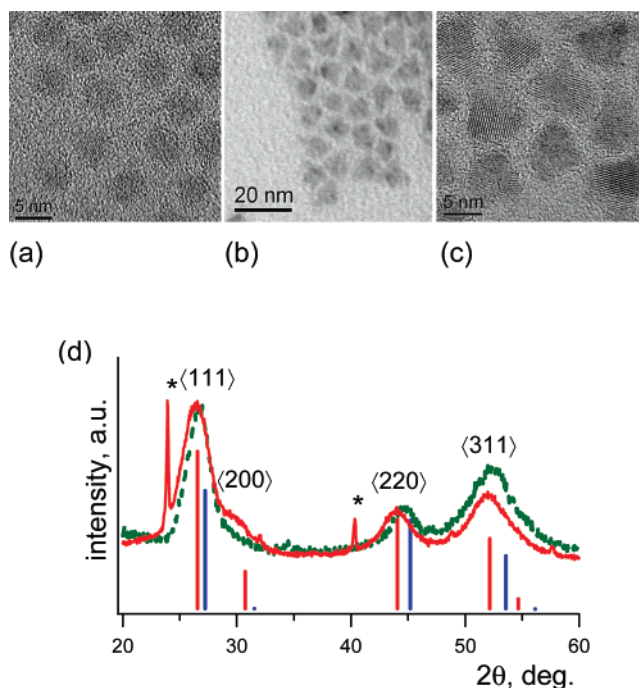
Figure 4. TEM images of CdS-core NCs (R = 2.4 nm) (a) and final CdS/ZnSe structures (diameter ca. 6.8 nm) following overcoating with ZnSe recorded in the low- (b) and high- (c) resolution modes. (d) XRD spectra of CdS-core (solid red line) and core/shell CdS/ZnSe (green dotted line) NCs along with XRD patterns of bulk cubic CdS (red bars) and bulk cubic ZnSe (blue bars). Impurity peaks are marked by asterisks.

(EDS) shows the presence of Zn and Se in a purified final product. Based on a statistical analysis of both particle dimensions and center-to-center separations (in the regions of close-packing), we estimate that hetero-NC diameters are from 6.8 to 7.5 nm and, hence, the ZnSe shell thickness, H, is 1.2 ± 0.2 nm. The results of XRD studies (Figure 4d) are consistent with the presence of ZnSe in the final heterostructures. The XRD pattern of core particles (Figure 4d, solid red line) matches that of bulk cubic CdS with no indication of the hexagonal phase formation. From the line width analysis of the ⟨220⟩ reflection peak using the Scherrer equation,[34] we estimate the average radius of CdS cores as 2.4 nm, which is in agreement with the TEM results. The XRD spectra of ZnSe overcoated samples also indicate the presence of only the cubic crystal phase (Figure 4d; dotted green line). However, all of the three major reflection peaks, ⟨111⟩, ⟨220⟩, and ⟨311⟩, shift to higher angles indicating a decreased average lattice parameter. This result is expected for CdS/ZnSe hetero-NCs, since the ZnSe lattice constant is smaller than that of cubic CdS (5.67 Å vs 5.81 Å, respectively). Additionally, we observe that the ⟨200⟩ peak of CdS almost disappears from the XRD spectra of the final heterostructures. This is also indicative of the formation of CdS/ZnSe NCs, as the intensity of the ⟨200⟩ reflection in pure ZnSe is normally negligibly small.

Despite the irregular shape of these hetero-NCs, we believe that the deposition of ZnSe occurs over the entire surface of CdS cores but not anisotropically along selected crystallographic directions. The core/shell NCs show no evidence of preferred orientation or alignment in XRD and TEM. The lack of any

(31) Peng, Z. A.; Peng, X. G. *J. Am. Chem. Soc.* **2001**, *123*, 183.
(32) Li, J. J.; Wang, Y. A.; Guo, W. Z.; Keay, J. C.; Mishima, T. D.; Johnson, M. B.; Peng, X. *J. Am. Chem. Soc.* **2003**, *125*, 12567.
(33) McBride, J.; Treadway, J.; Feldman, L. C.; Pennycook, S. J.; Rosenthal, S. J. *Nano Lett.* **2006**, *6*, 1496.
(34) Cullity, B. D. *Elements of X-Ray Diffraction*; Addison-Wesley: Reading, MA, 1978.
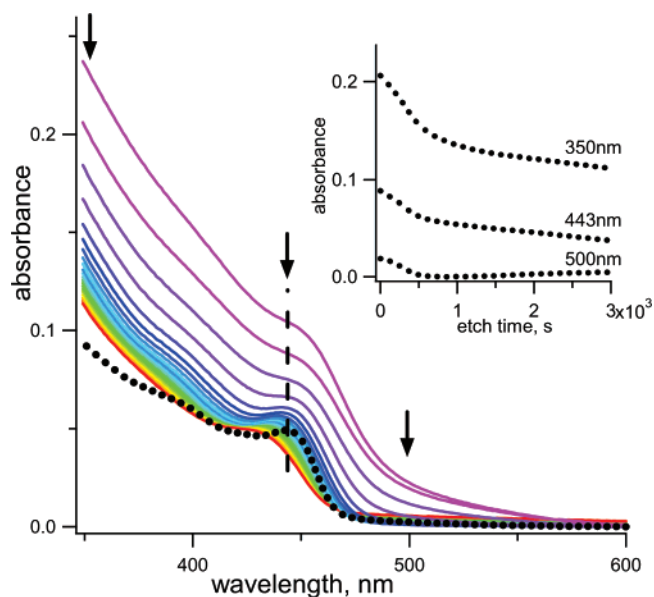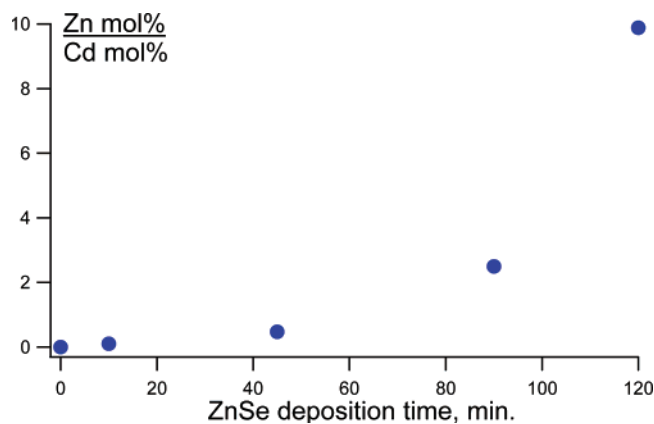
Figure 5. Evolution of absorption spectra of CdSe/ZnSe/BzNH$_2$ NCs (solid lines with colors from purple to red) during etching with BPO. The spectra were taken in 2.5 min intervals. The absorption spectrum of the original CdS core sample is shown by the black dotted line; the band edge transition is indicated by the black dashed line at 443 nm. The inset shows the dependence of absorbance on etching time at three wavelengths marked by black arrows in the main panel. The change in the slope of these dependences clearly indicates the transition between two different etching stages; the initial fast change in absorbance is associated with removal of the ZnSe shell, while the second stage with slower changes in absorbance is due to dissolution of the CdS core.

Figure 6. Apparent Zn-to-Cd molar ratio in CdS/ZnSe NCs as determined from Zn 2p and Cd 3d XPS signal intensities (see text) presented as a function of ZnSe shell deposition time, which is directly proportional to the Zn-to-Cd molar ratio in the reaction product.

systematic shape anisotropy (as in the case of, e.g., rod-shaped heterostructures) is also indicated by the fact that hetero-NCs form well-ordered hexagonal patterns in the regions of close-packing in TEM images (Figure 4b). Furthermore, the hetero-NC emission wavelengths measured experimentally can be accurately modeled assuming a spherically symmetric core/shell arrangement of CdS and ZnSe (see spectroscopic analysis below).

To confirm the core/shell architecture of synthesized NCs, we have performed controlled etching of CdS/ZnSe NCs with BPO and also conducted their XPS analysis for different ZnSe shell thicknesses. Figure 5 shows the evolution of absorption spectra of synthesized NCs during the etching procedure. These data clearly indicate two etching stages. During the first stage, the red tail of the absorption spectrum disappears, which is accompanied by the development of a sharp band-edge peak at higher energies. The peak position is close to that of the original CdS-core sample used to grow the CdS/ZnSe core/shell NCs. During the second stage, the etching rate becomes significantly lower as indicated by slowed changes in absorption spectra. The reduction in the magnitude of the absorption coefficient is accompanied by the blue shift of the band-edge feature and its broadening.

As expected from selenium and sulfur positions in the periodic table[35] and as it was observed experimentally,[26,36] selenides undergo oxidation easier than sulfides. Therefore, fast changes in absorption at the initial etching stage can be explained by rapid dissolution of the ZnSe shell. This explanation is consistent

with the disappearance of a red tail in the absorption spectra, which originates from a spatially indirect transition coupling a hole state in the ZnSe shell with an electron state in the CdS core. After the shell is removed, this weak indirect transition is replaced with a strong spatially direct transition in a CdS core, which results in the development of a sharp band-edge absorption feature as observed experimentally.

After the shell is completely removed and BPO reaches the less reactive CdS surface, the etching rate should slow down as indeed observed experimentally (Figure 5) for the second stage of NC etching. The blue shift of the band-edge transition at this stage is due to reduction in the size of CdS NCs. Controlled experiments with varied concentrations of BPO confirmed that the decrease in the etching rate during the second stage is not caused by the deficit of the peroxide.

To complement the results of chemical etching experiments, we have conducted the XPS study of CdS/ZnSe core/shell NCs for a fixed core size and varied shell thicknesses. XPS survey scans were recorded for the entire range of binding energies of atomic core levels of the sample to evaluate both overall composition of the NCs and to identify regions on the HOPG surface where the NC population was spatially continuous and suitable for a more quantitative determination of composition (not shown). These initial studies were followed by higher resolution scans for Cd 3d, Zn 2p, and Se 3d levels. The observed binding energies of different core levels were consistent with literature data for NCs.[37,38] The Cd 3d$_{5/2}$ peak in the core/shell structure was typically located between 406.4 and 406.5 eV, the Zn 2p$_{3/2}$ level peak position was in the range 1023.0−1023.3 eV, and the Se 3d peak was at 55.5−55.6 eV. We observed that the ratio of the Zn 2p$_{3/2}$ to Cd 3d$_{5/2}$ signal integral intensities measured by Mg Kα excitation steadily increased with increasing ZnSe shell deposition time which is proportional to the increase in the Zn:Cd molar ratio in the reaction product (Figure 6). Furthermore, the Zn-to-Cd apparent molar ratio (calculated from the ratio of Zn 2p to Cd 3d signal intensities corrected by the corresponding XPS spectrometer manufacturer's sensitivity factors) showed a superlinear increase with the shell deposition time, which argues that the growth of
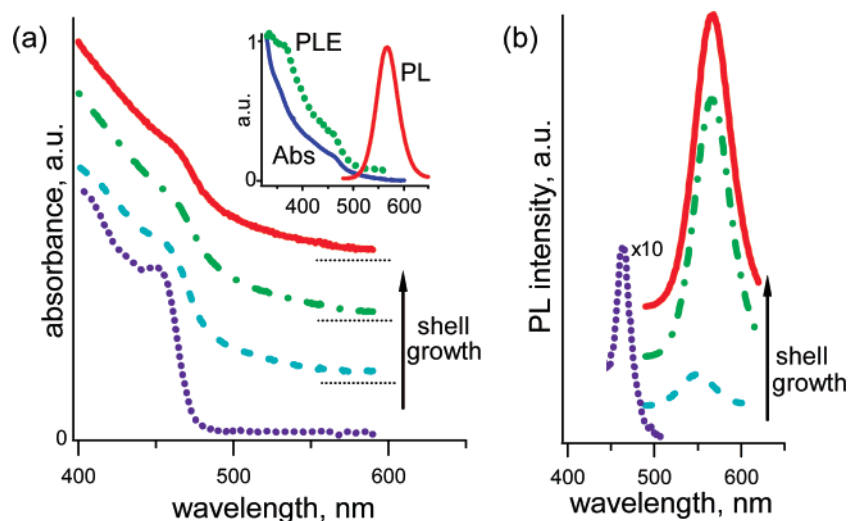
(35) Greenwood, N. N.; Earnshaw, A. *Chemistry of the Elements, 2nd ed.*; Butterworth-Heinemann: Oxford, U.K., 1997.
(36) Dimitrijević, N. M.; Kamat, P. V. *Radiat. Phys. Chem.* **1988**, *32*, 53.

(37) Bowen Katari, J. E.; Colvin, V. L.; Alivisatos, A. P. *J. Phys. Chem.* **2001**, *90*, 2504.
(38) Nanda, J.; Sapra, S.; Sarma, D. D. In *Encyclopedia of Nanoscience and Nanotechnology*; Nalwa, H. S., Ed.; American Scientific Publisher: 2004.

Figure 7. Evolution of optical absorption (a) and emission (b) spectra of CdSe/ZnSe NCs during the growth of the shell (the spectra are offset vertically for clarity). The bottom spectra in (a) and (b) (purple dotted lines) correspond to core-only CdS NCs ($\lambda_o = 470$ nm). Absorption and PL spectra shown by the same color and style correspond to the same samples. Inset: Absorption (blue solid line), PLE (green dotted line), and PL (red solid line) spectra of the sample with the thickest shell [top spectra in (a) and (b)]. The PLE signal is collected at the center of the emission band (567 nm).

the Zn-containing component of a hetero-nanostructure leads to signal attenuation, due to inelastic photoelectron scattering of the underlying Cd component. This is exactly the trend expected for a growth of a well-defined ZnSe shell on top of a CdS core.

Figure 7 shows the evolution of optical absorption (panel a) and emission (panel b) spectra of NCs during the growth of the ZnSe shell on CdS cores emitting at 470 nm. The pure CdS NCs show a sharp lowest-energy 1S absorption peak at 460 nm. The growth of the ZnSe shell leads to broadening of the 1S feature and the development of a low-energy tail, which extends past 550 nm for thick shells. This behavior is consistent with the formation of a type-II structure that exhibits new absorption features due to weak spatially indirect transitions with energies that are lower than the pure-CdS-core energy gap. A similar behavior was observed previously in studies of the type-I to the type-II transition in inverted ZnSe/CdSe NCs.[15]

Clear signatures of formation of type-II structures are also observed in PL spectra (Figure 7b). Pure CdS core particles exhibit emission at 470 nm. Addition of Zn/Se precursors causes almost immediate quenching of this band, which likely occurs as a result of a disturbance of surface passivation accompanied by the formation of a large number of surface traps. As the ZnSe shell grows thicker, we observe the development of a new emission feature at 550 nm, which becomes more intense with increasing shell width. This new band experiences a red shift with shell growth until its wavelength "saturates" at 581 nm.

The inset of Figure 7a shows the PL excitation (PLE) spectrum of CdS/ZnSe NCs (corresponding to the sample with the thickest shell in the main panel of Figure 7a) acquired by monitoring the PL intensity as a function of the photoexcitation wavelength. The useful feature of the PLE technique is that by comparing PLE and absorption spectra one can, in principle, detect the presence of nonemitting species (they contribute to absorption but not PLE) or distinguish between several emitting species that might have similar emission wavelengths but spectrally distinct excitation channels. For core/shell samples studied here, we observe close correspondence between absorption and PLE traces. This result indicates that all photoexcita-

tions harvested across the entire range from ~550 to ~300 nm are funneled into the lowest-energy indirect exciton state, and the decay of this state produces the PLE signal through the radiative decay component. From a chemistry perspective, this observation implies that our core/shell NC synthesis does not generate significant amounts of byproducts such as pure CdS, ZnSe, or CdSe NCs that would produce distinct spectral features in absorption spectra without contributing to PLE.

To analyze our spectroscopic results, we use the model described in section 3. In Figure 8a, we show the shell-width dependence of the hetero-NC emission wavelength calculated assuming that the initial PL wavelength (core-only NCs) is 470 nm, which corresponds to the experimental situation in Figure 7. PL quenching at the early stage of shell growth prevents us from observing experimentally a continuous shift of the emission maximum with increasing H. However, the large-H wavelength limit predicted by our modeling (595 nm) is close to the 581-nm "saturation" wavelength measured experimentally (the top spectrum in Figure 7b). Based on good correspondence between measured and calculated emission energies for two different limits ("no shell" and "thick shell"), we can assume that the theoretical dependence is also accurate for intermediate shell thicknesses. In this case, the emission wavelength of 550 nm, for which PL becomes first detectable during the shell growth, should correspond to $H \approx 1.6$ nm. This value represents the minimum shell thickness at which the CdS/ZnSe interface becomes sufficiently trap-free to allow development of the band-edge emission from the heterostructure. According to the diagram in Figure 3, this thickness corresponds to the true type-II regime, in which the hole is localized in the shell. In this case, its wavefunction is close to zero at the CdS/ZnSe interface, which likely also contributes to reducing interactions with interface defects and facilitates the development of the band-edge emission.

Good correspondence between calculated and measured initial (no shell, λ_o) and final (thick shell, λ_{final}) emission wavelengths is also observed for other CdS-core sizes. For example, the inset of Figure 8a shows that the core with the original emission at 426 nm eventually produces PL at 551 nm following overcoating
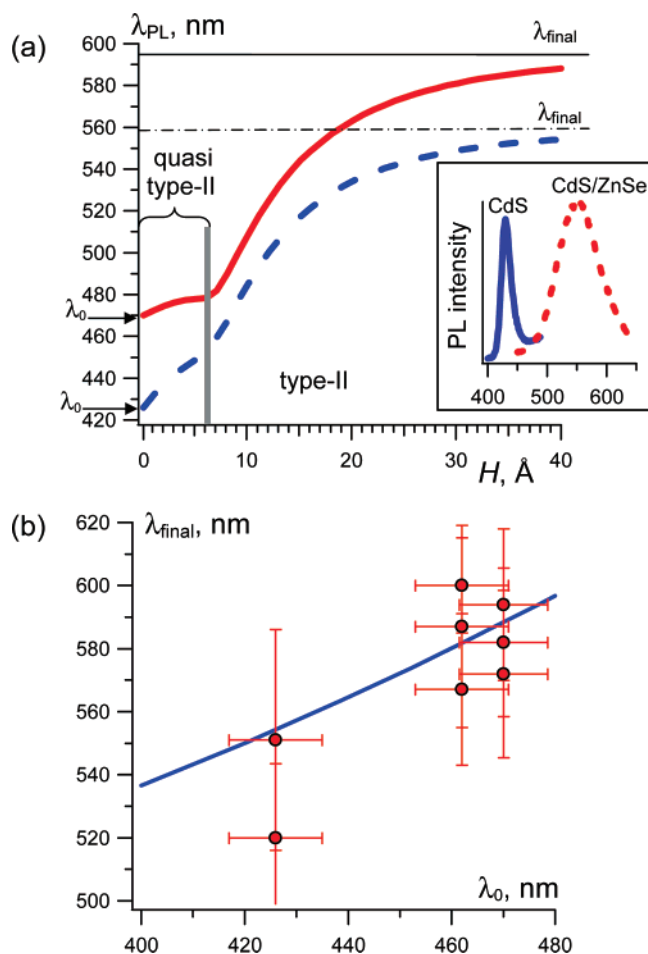
Figure 8. (a) Calculated emission wavelength as a function of H for CdS/ZnSe NCs with two different CdS-core radii that correspond to initial emission wavelengths ($H = 0$) of 470 nm (red solid line) and 426 nm (blue dashed line). The vertical gray bar marks the shell thickness, which corresponds to the transition between the quasi type-II and the true type-II regimes (it is nearly identical for cores with emission wavelengths of 470 and 426 nm). Inset: the PL spectra of small CdS cores (blue solid line) and the resulting core/shell NCs with a thick shell (red dash line). (b) Comparison of the measured (red circles) and the calculated (blue line) dependence of the final emission wavelength λ_{final} (large-H limit) of CdS/ZnSe NCs on the initial wavelength λ_o ($H = 0$) of CdS cores. Error bars represent half widths of the hetero-NC PL spectra measured at half-height. Vertically aligned data points correspond to different core/shell samples fabricated using CdS cores with the same emission wavelength. Variations in the emission wavelength of the final hetero-NCs are likely due to slight variations in the sharpness of the CdS/ZnSe interface (induced, e.g., by uncontrolled alloying).

with ZnSe. This peak slightly red shifts to 567 nm as the ZnSe shell grows thicker. The final value of the emission wavelength is close to the calculated saturation wavelength of 558 nm (dash line in Figure 8a). More data points that compare experimental and theoretical values of the initial and final wavelengths are given in Figure 8b.

Qualitative behaviors of measured absorption, PL, and PLE spectra as well as quantitative comparison with results of theoretical modeling provide strong evidence that synthesized heterostructures indeed exhibit type-II localization as expected from the alignment of energy states at the CdS/ZnSe interface. Furthermore, based on a good agreement between calculated and measured transition energies, we can use the emission wavelengths observed for synthesized structures for quantifying the degree of spatial separation in terms of the e−h overlap
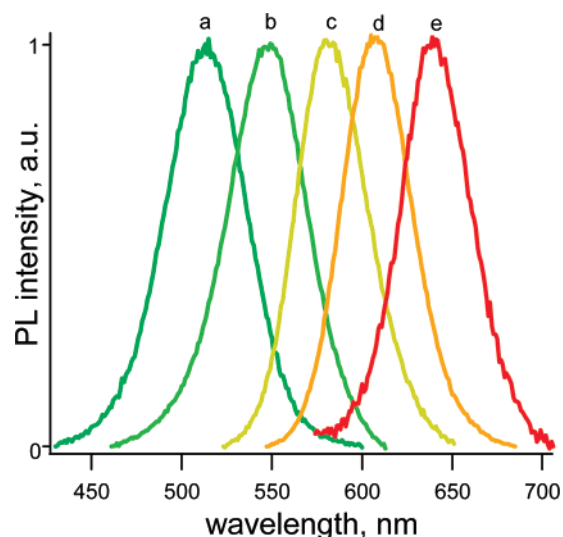

Figure 9. PL spectra of a series of CdS/ZnSe core/shell NCs grown using CdS cores emitting at 426 nm (samples a and b) and 470 nm (samples c−e). Samples a−c have a sharp CdS/ZnSe interface, while samples d and e have an intermediate ZnCdSe layer formed by treating CdS cores with Cd(II) in the amounts of 2% (d) and 10% (e) of Zn(II) used during the shell deposition. Presented data illustrate the possibility of wide spectral tunability of the emission color (from red to green in this example) by combining control of the core size, the shell width, and the interface composition.

integral, Θ, based on diagrams in Figure 3. For example, for samples in Figure 7 the initial emission wavelength (core-only sample) is 470 nm, which indicates (according to Figure 3a) that in this structure the core radius is sufficiently large ($R > R_c$) to produce a core-localized electron state for any value of H. During the shell growth, the detectable PL signal first develops at 550 nm. By mapping this 550-nm data point from Figure 3a to Figure 3b, we can estimate that the corresponding value of the e−h overlap integral is between 0.05 and 0.1, indicating almost complete spatial separation between electrons and holes in this sample, consistent with the true type-II regime. Further increase in the shell thickness improves the separation between positive and negative charges, and according to our model, Θ drops to, or even below, 0.05 for the thickest shells synthesized here.

In structures synthesized in this work, an electron is localized in the core independent of the value of H. Therefore, the control of the shell thickness alone does not provide significant spectral tunability of the emission wavelength (see Figure 3a), especially because PL is suppressed for thin shells. In this situation, extension of the range of spectral tunability is possible by using different core sizes and/or different degrees of CdS/ZnSe interface alloying. An example in Figure 9 shows that with CdS cores emitting at 426 nm and 470 nm, one can tune the PL wavelength from ∼520 to ∼650 nm (corresponding to changes in the emission color from green to red) by controlling the shell thickness and interface composition.

4.4. Alloying the CdS/ZnSe Interface. An important parameter of NCs, especially from the point of view of practical applications, is the emission efficiency. The factor that limits the PL efficiency in monocomponent core-only NCs is recombination through surface defects. In the case of core/shell structures an additional source of defect sites is the core/shell interface.[25] As synthesized, the hetero-NCs described above show PL QYs up to 10−15%, which is already relatively high
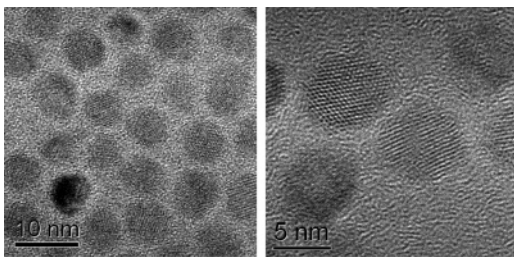
Figure 10. Low- (left) and high- (right) resolution TEM images of heavily alloyed CdS/ZnSe NCs synthesized using the same CdS cores as those shown in Figure 4a.

for colloidal systems without any special treatment of the NC surfaces. In our attempt to obtain even higher QYs, we studied the effect of alloying the CdS/ZnSe interface on PL efficiencies. We believe that our procedure of introducing Cd(II) in the solution of CdS cores prior to deposition of the ZnSe shell (see section 2.6) leads to the formation of an interfacial layer of the ZnCdSe solid solution. The lattice constant of ZnSe (5.67 Å) is smaller than that of CdS (5.83 Å). The addition of Cd to ZnSe increases the lattice constant of the resulting solid solution.[39,40] Specifically, the lattice constant of $Zn_{0.7}Cd_{0.3}Se$ is expected to closely match that of CdS.[40] Therefore, introduction of the ZnCdSe intermediate layer can, in principle, improve the lattice matching at the core/shell interface and, hence, reduce the number of interfacial defects.

To initiate the growth of the intermediate ZnCdSe layer, we introduced extra $Cd(AcO)_2$ solution in TOP in the reaction mixture containing CdS cores prior to the addition of the ZnSe precursors. The amount of extra Cd(II) was varied from approximately 1% to 10% of the amount of Zn(II) used in the synthesis of the ZnSe shell. Since CdSe is thermodynamically more stable than ZnSe with regard to dissociation, addition of Zn/Se precursors in the presence of the Cd(II) source is expected to first initiate the formation of $Zn_xCd_{1-x}Se$ solid solution on the surface of the CdS cores. As the reaction proceeds and the amount of available Cd(II) decreases, the shell composition gradually changes from ZnCdSe solid solution to pure ZnSe.

The above alloying procedure conducted even with small amounts of $Cd(AcO)_2$ (1−2%) resulted in almost double the QY of the final core/shell NCs (best samples showed PL QY up to 50%). The TEM images and XRD spectra of these lightly alloyed samples were similar to those of samples without alloyed interfaces. The addition of large amounts of $Cd(AcO)_2$ (7−10%) did not lead to further improvements in QY; however, it had a distinct effect on both XRD and TEM results. Specifically, the XRD spectra of heavily alloyed samples clearly indicate the presence of hexagonal CdSe (not shown), which is consistent with the formation of an intermediate graded shell composed of a solid solution of CdSe and ZnSe. TEM images (Figure 10) indicate that heavily alloyed NCs have nearly spherical shapes and exhibit narrower dispersity compared to samples fabricated without alloying (Figure 4). In the example in Figure 10, the mean particle diameter is 6.8 and the size dispersion is ∼12%.

Another approach to forming an intermediate solid-solution layer studied here involved the use of partially purified CdS cores that contained some amount of surface adsorbed Cd(II)

(see section 4.1). This approach also produced improved PL QYs, but because of the difficulty in controlling the amount of Cd(II) on the CdS NC surfaces by purification procedures, this method provided less control over formation of the intermediate layer compared to that utilizing thoroughly purified CdS cores and $Cd(AcO)_2$ as a well-defined source of Cd(II).

5. Conclusion

In conclusion, we have developed synthetic procedures for the fabrication of highly luminescent colloidal CdS(core)/ZnSe-(shell) hetero-NCs that can produce a type-II carrier localization regime by spatially separating electrons and holes between the core and the shell, respectively. The emission wavelength of these NCs can be controlled by varying both core radius and shell width, and for samples studied here it changes from 500 nm (green) to 650 nm (red). The PL QY of hetero-NCs with a sharp core/shell interface is up to 15%, and it can be further tripled by alloying the interfacial layer of ZnSe with a small amount of CdSe. The latter approach likely leads to reduction of the number of defects at the CdS/ZnSe boundary. We have also developed a theoretical model for describing the band-edge states in CdS/ZnSe core/shell NCs, which takes into account both direct e−h coupling and interface-polarization effects. We observed good correspondence between calculated and measured energies of the band-edge transition in hetero-NCs with various core radii and shell widths. We further used this model to estimate the degree of spatial separation between electrons and holes (quantified in terms of the electron−hole overlap integral, Θ) as a function of the emission wavelength. Depending on the shell width, the value of Θ varies from 0.2−0.3 to below 0.05, indicating nearly complete separation between electron and hole wavefunctions, which is consistent with the true type-II localization regime.

One potential application of these type-II NCs is in optical amplification and lasing.[16,41] Because of the multiexciton nature of optical gain in NCs,[16,42] realization of the lasing regime using colloidal materials is significantly complicated by ultrafast nonradiative Auger recombination of multiexcitons, which results in short, picosecond lifetimes of optical gain.[41,43] The most radical approach to solving the problem of Auger recombination is through the development of structures that would allow obtaining lasing in the single-exciton regime for which Auger recombination is inactive. One such approach, first discussed in ref 15 involves realization of strong exciton−exciton (X−X) repulsion, which can raise the energy of the competing absorbance in singly excited NCs relative to the emission line. This concept, however, cannot be realized using traditional type-I NCs, in which the X−X interaction is attractive and hence the X−X interaction energy (Δ_{XX}) is negative.[44] On the other hand, by spatially separating electrons and holes one can increase the repulsive component of the interaction energy, which can change the sign of Δ_{XX}. As demonstrated in our modeling of biexciton states in type-II core/shell NCs, hetero-

(39) Fedorov, V. A.; Ganshin, V. A.; Korkishko, Yu, N. *Mater. Res. Bull.* **1992**, *27*, 877.
(40) Bouroushian, M.; Kosanovic, T. *J. Solid State Electrochem.* **2006**, *10*, 223.

(41) *Semiconductor and Metal Nanocrystals: Synthesis and Electronic and Optical Properties*; Klimov, V. I., Ed.; Marcel Dekker: New York, 2003.
(42) Mikhailovsky, A. A.; Malko, A. V.; Hollingsworth, J. A.; Bawendi, M. G.; Klimov, V. I. *Appl. Phys. Lett.* **2002**, *80*, 2380.
(43) Klimov, V. I.; Mikhailovsky, A. A.; Xu, S.; Malko, A.; Hollingsworth, J. A.; Leatherdale, C. A.; Eisler, H. J.; Bawendi, M. G. *Science* **2000**, *290*, 314.
(44) Achermann, M.; Hollingsworth, J. A.; Klimov, V. I. *Phys. Rev. B* **2003**, *68*, 245302.

structures with a sufficiently small e−h overlap (Θ < 0.2) can produce very strong X−X repulsion characterized by "giant" values of Δ_{XX} of ca. 100 meV or greater.[45] This result was recently confirmed by our experimental studies of X−X interactions in CdS/ZnSe NCs, which indicated large repulsion energy up to 106 meV.[46] The latter value is comparable to a transition line width in typical NC samples implying the possibility of almost complete suppression of absorption at the position of the emitting transitions in NCs excited with a single exciton. Recently, we used CdS/ZnSe NCs described in this work to demonstrate both optical gain and amplified spontaneous emission in the single-exciton regime.[46]

Supporting Information Available: Detailed description of the theoretical model used in this work. This material is available free of charge via the Internet at http://pubs.acs.org.

JA068351M

(45) Piryatinski, A.; Ivanov, S. A.; Tretiak, S.; Klimov, V. I. *Nano Lett.* **2007**, *7*, 108.

(46) Klimov, V. I.; Ivanov, S. A.; Nanda, J.; Achermann, M.; Bezel, I.; McGuire, J. A.; Piryatinski, A. *Nature* **2007**, *447*, 441.